# Surface plasmon polaritons at a metal-dielectric interface with randomly spaced subwavelength holes

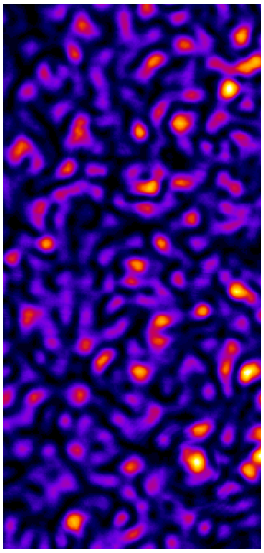


| | |
|---|---|
| *Author:* | Anne Meeussen |
| *Thesis type:* | Physics bachelor thesis |
| *Supervisors:* | Frerik van Beijnum |
| | Martin van Exter |
| *Research group:* | Quantum Optics |
| *Institute:* | Leiden Institute of Physics |
| *Faculty:* | Faculty of Science |
| *University:* | Leiden University |
| *Date:* | August 27, 2012 |

# Contents

# 1 Introduction

In this thesis, research is presented in which we investigate the properties of surface plasmon polaritons (SPPs) and the presence of other surface waves on a metal-dielectic interface. The theoretical existence of surface plasmons, which are oscillations of the free electron density at a metal surface, was first demonstrated in the late 1950s [1]. An SPP is a resonant coupling between such a surface plasmon and an electromagnetic field [2]. This resonant coupling is illustrated in figure 1. An SPP [1]can thus be excited by light, and in a reverse process it can also couple out as light. Normal to the metal-dielectric interface, the SPP is bound and therefore the SPP-field is evanescent as shown in figure 1; however, parallel to the interface the SPP propagates as a surface wave. The 1960s and 1970s saw the development of basic experimental methods still in use today [2] to optically excite these SPPs at metal-dielectric interfaces, using prisms [3, 4], periodic metal gratings [5] and surface defects [6]. In subsequent years, the potential use of SPPs in practical applications was recognised. For example, SPPs can be controlled with subwavelength structures and therefore SPPs are useful in nanophotonic circuits [7, 8]. SPPs are also used in sensing applications; sensors based on SPP activity are widely researched and used commercially today [9]. The promise of practical applications for SPPs has thus stimulated fundamental and applied research, which has experienced a large growth since the early 1990s [10].

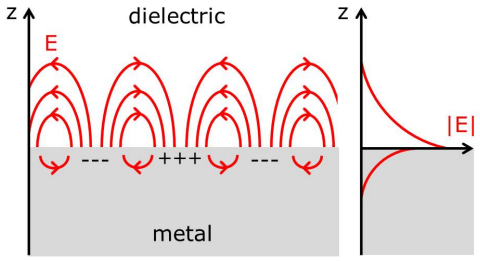


*Figure 1: Schematic representation of a surface plasmon polariton at a metal-dielectric interface. Normal to the interface, the SPP is bound and its field is evanescent. Adapted from Barnes et al. [2].*

Our research has its conceptual roots in the late 1990s, when Ebbesen et al. [11] observed that the transmission spectra of metal films with subwavelength holes contain much larger maxima than predicted by standard aperture theory [12]. Such extraordinary optical transmission is due to SPP-mediation: light incident on a hole in a metal film excites an SPP, which propagates over the film and in turn couples out as light at another hole. In addition, recent theoretical [13, 14] and experimental work [13, 15] has shown that besides SPPs, two other surface waves contribute to the extraordinary optical transmission at short and long distance regimes: the quasicylindrical wave and the Norton wave.

In this thesis we research the properties of SPPs by studying the transmission of light through metal-dielectric samples with randomly spaced subwavelength holes. The transmission of light through such a sample results in a random interference pattern (often called speckle pattern). Light is transmitted directly through the holes and indirectly via SPP-mediation [16]. Thus, both the directly and indirectly transmitted light contribute to the total speckle pattern. As we tune the wavelength of the incident light, we expect the two contributions to show a different wavelength-dependence: the SPP contribution decorrelates after a wavelength detuning of tens of nanometers, and the direct contribution is practically constant [17, 18]. We use this difference to separate the contributions by calculating the correlation of the speckle patterns as a function of wavelength. From this correlation function, we extract information about the losses of the SPPs as they propagate over the surface and about the relative strength of the direct and indirect transmission processes. We perform this experiment for multiple samples, each with a different hole density. At very high and very low hole densities we hope to see contributions from the quasicylindrical and Norton waves. The experiments presented here are a continuation of research done in 2011 [17, 18]. In our study we use a different light source, extending the potential wavelength tuning range from 70 nm to roughly 400 nm.

In Chapter 2, we present a theoretical model for the speckle patterns. With this model we calculate the theoretical correlation of the speckle patterns during wavelength detuning, and we discuss what information on SPPs and other surface waves we can extract. Chapter 3 describes the setup and samples used to measure speckle patterns. Chapter 4 addresses how we prepare the recorded speckle patterns for correlating. In Chapter 5 we then present our

[1]Please note that this research only deals with SPPs; for convenience, the terms 'surface plasmon polariton' and 'surface plasmon' will be used interchangeably and may be abbreviated to 'plasmon' from Chapter 2 onwards.

experimental correlation functions, compare them to the model, and present the extracted information about SPPs and other surface waves. Finally, we discuss the conclusions drawn from the experimental results and present an outlook on further research in Chapter 6.

# 2 Theory

We wish to look at the properties of surface plasmon polaritons by studying far-field interference patterns of light transmitted through metal-dielectric samples with randomly spaced subwavelength holes as we tune the wavelength of the incident light. In this Chapter we will present our theoretical model [16, 17, 18] for this experiment. We argue that light is transmitted through the sample in two ways: light may pass directly through the holes and it may pass through the sample indirectly via surface plasmons (section 2.1). A model for the plasmon-mediated transmission is presented (section 2.2). We then calculate the theoretical correlation of the transmission as a function of wavelength detuning and show that this correlation function yields information about the transmission processes (section 2.3). Finally, the potential contribution of non-plasmon surface waves to the transmission is discussed (section 2.4).

## 2.1 Direct and indirect transmission of light through randomly spaced subwavelength holes

In this section we present a theoretical model of the far-field transmission of light through a metal-dielectric sample with randomly spaced subwavelength holes. Just as light transmitted through a sample with ordered hole patterns produces an ordered interference pattern, a sample with randomly spaced holes produces a random interference pattern, often denoted speckle pattern. We look at this interference pattern at an angle $|\vec{\theta}|$ in the far-field, as illustrated in figure 2. For a single hole $i$ at position $\vec{r}_i$, the transmitted light at the sample surface is described by some field $E_i$; in the far-field, this $E_i$ acquires a phase factor $e^{i\vec{k}_{||}\cdot\vec{r}_i}$. In this expression, $\vec{k}_{||}$ is the component of the wave vector $\vec{k}_0$ parallel to the sample surface so that $k_{||} = \frac{2\pi}{\lambda}\sin(|\vec{\theta}|)$, where $\lambda$ is the free space wavelength of the incident light. Since the hole positions are random, the phase factor is statistically independent for different holes.

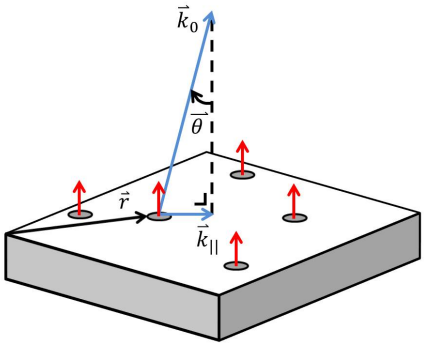


*Figure 2: Schematic representation of light transmitted via holes in a sample to a point in the far-field. $\vec{r}$ is the hole position; $\vec{k}_0$ is the wave vector of the light; $\vec{k}_{||}$ is the component of the wave vector parallel to the sample surface.*

Light is transmitted through the sample by two means: it either passes directly through a hole, or light incident at one hole excites a surface plasmon which propagates over the surface and couples out as light at another hole. In the far-field the directly transmitted light is given by $E_{d,i}e^{i\vec{k}_{||}\cdot\vec{r}_i}$ for a single hole $i$. Because the holes are identical, we assume that the direct field strength is the same at each hole: $E_{d,i} = E_d$. The indirectly transmitted light due to plasmon mediation is given by $E_{s,i}e^{i\vec{k}_{||}\cdot\vec{r}_i}$. The plasmon-mediated contribution at a single hole involves excitation at all other holes which are randomly positioned, and we therefore assume that the indirect field $E_{s,i}$ has a random phase which is uncorrelated to its amplitude. Hence, the indirect fields at different holes are statistically independent. We also assume that the direct and indirect transmission processes are uncorrelated so that $E_d$ and $E_{s,i}$ are statistically independent. The total transmitted light in the far-field is then given by the summation of direct and indirect contributions over $N$ holes:

$$E = \sum_i^N \left[E_d + E_{s,i}\right] e^{i\vec{k}_{||}\cdot\vec{r}_i} \tag{1}$$

We are interested in the mean intensity of the total transmitted light, which we will later use to calculate the correlation of the speckle pattern at different wavelengths. We calculate the mean intensity by performing an ensemble average of the absolute squared value of the field (see equation 1). Keeping in mind that $\langle\sum\cdot\rangle = \sum\langle\cdot\rangle$

and that $\langle AB\rangle = \langle A\rangle \langle B\rangle$ for statistically independent quantities $A$ and $B$, we write the mean intensity in terms of the fields at each hole:

$$\langle I\rangle = \langle |E|^2\rangle = \sum_{i,k}^{N} \left[\langle E_d E_d^*\rangle + \left\langle E_{s,i}E_{s,k}^*\right\rangle + \left\langle E_d E_{s,k}^*\right\rangle + \langle E_{s,i}E_d^*\rangle\right] \left\langle e^{i\vec{k}_{||}\cdot(\vec{r}_i-\vec{r}_k)}\right\rangle \tag{2}$$

To further evaluate this expression we will consider each term separately. First we consider the cross terms between direct and indirect fields: $\langle E_d E_{s,k}^*\rangle$ and $\langle E_{s,i}E_d^*\rangle$. The direct and indirect fields are statistically independent; moreover the mean indirect fields $\langle E_{s,k}\rangle$ and $\langle E_{s,i}\rangle$ go to zero since their phase is random and uncorrelated to their amplitude, and hence both $\langle E_d E_{s,k}^*\rangle$ and $\langle E_{s,i}E_d^*\rangle$ are zero. Secondly we look at the term with only indirect fields: $\langle E_{s,i}E_{s,k}^*\rangle$. The fields at different holes $i \neq k$ are statistically independent and the mean indirect fields $\langle E_{s,i}\rangle$ and $\langle E_{s,k}\rangle$ go to zero as before, leaving only terms for identical holes $i = k$. For these terms, the random phase factor $\langle e^{i\vec{k}_{||}\cdot(\vec{r}_i-\vec{r}_k)}\rangle$ is equal to one. Lastly, we evaluate the term with only direct fields :$\langle E_d E_d^*\rangle$. For $k_{||} \neq 0$ (outside the zeroth-order) the random phase factor $\langle e^{i\vec{k}_{||}\cdot(\vec{r}_i-\vec{r}_k)}\rangle$ goes to zero at different holes $i \neq k$ and equals one at identical holes $i = k$, leaving only terms for identical holes. Since all terms in equation 2 for $i \neq k$ are zero, the double summation is replaced by a single summation over $N$ holes. Thus, the mean intensity outside the zeroth-order is:

$$\text{for } k_{||} \neq 0: \qquad \langle I\rangle = \sum_{i}^{N} \left[\left\langle |E_d|^2\right\rangle + \left\langle |E_{s,i}|^2\right\rangle\right] = N|E_d|^2 + N\left\langle |E_s|^2\right\rangle, \tag{3}$$

where we have replaced the summation of ensemble averages by N times the ensemble average.

Now we evaluate the mean intensity at $k_{||} = 0$ (zeroth-order transmission). The previous analysis only changes for the direct term $\langle E_d E_d^*\rangle$ as the phase factor $\langle e^{i\vec{k}_{||}\cdot(\vec{r}_i-\vec{r}_k)}\rangle$ is then always equal to one. Therefore the direct term contains a double summation over $N$ holes rather than the single summation found previously. Hence, the mean intensity in the zeroth-order is:

$$\text{for } k_{||} = 0: \qquad \langle I\rangle = \sum_{i,k}^{N} \langle E_d E_d^*\rangle + \sum_{i}^{N} \left\langle |E_{s,i}|^2\right\rangle = N^2|E_d|^2 + N\left\langle |E_s|^2\right\rangle \tag{4}$$

Equations 3 and 4 show that in the zeroth-order transmission ($k_{||} = 0$) the direct transmission dominates strongly; outside the zeroth-order transmission ($k_{||} \neq 0$) the direct and indirect contributions are typically of the same order of magnitude. We wish to study the indirect contribution and therefore we perform our experiments outside the zeroth-order.

## 2.2 Surface plasmon model of the indirect transmission

To study the indirect contribution $\left\langle |E_s|^2\right\rangle$ to the mean transmitted intensity we now formulate a model for the plasmon-mediated field $E_{s,i}$ at a hole $i$ on a metal-dielectric interface. We assume that surface plasmons excited at all holes $j$ propagate in a straight line toward hole $i$ and couple out there as illustrated in figure 3. This model is expressed as:

$$E_{s,i} = \sum_{j} \frac{A_0(\phi_{ij})}{\sqrt{r_{ij}}} e^{(-\sigma\rho + ik_{\text{spp}})r_{ij}} \tag{5}$$

Where we perform a summation over all holes $j$ to account for each plasmon contribution at hole $i$. Here, $r_{ij}$ is the distance between holes i and j; $\sigma$ is the amplitude scattering cross section for a surface plasmon at a hole; $\rho$ is the hole density; $k_{\text{spp}}$ is the complex surface plasmon wave number, which can be expressed in terms of the free space wave number $k_0$ and the effective refractive index $n_{\text{eff}}$ of the metal and the dielectric medium as $k_{\text{spp}} = k_0 n_{\text{eff}}$; $\phi_{ij}$ is the angle between the incident light polarization and the plasmon propagation direction [19]; and $A_0(\phi_{ij})$ describes both the plasmon excitation efficiency at hole $j$ and the light outcoupling efficiency at hole $i$. The factor $\frac{1}{\sqrt{r_{ij}}}$ reflects

the amplitude reduction of a two-dimensional cylindrical wave after propagating over a distance $r_{ij}$ between holes $j$ and $i$. The phase factor of the plasmon field is given by $e^{i\text{Re } k_{\text{spp}} r_{ij}}$ and the amplitude of the plasmon field is given by $e^{-(\sigma\rho+\text{Im } k_{\text{spp}})r_{ij}}$. Traveling from hole $i$ to hole $j$ (see figure 3) a plasmon may encounter another hole and scatter out part of its field, which is modeled as $e^{-\sigma\rho r_{ij}}$. The plasmon may also be absorbed by the sample; the typical amplitude absorption length is Im $k_{\text{spp}} = l_{abs}^{-1}$. Therefore, the plasmonic amplitude losses due to scattering by the holes and absorption into the sample are given by: $loss = \sigma\rho + l_{abs}^{-1}$.

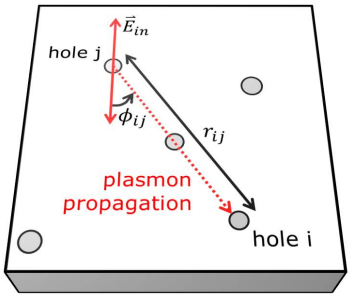


*Figure 3: Plasmon-assisted transmission of light in a sample with randomly spaced holes. Incoming polarized light $\vec{E}_{in}$ excites a surface plasmon at hole $j$ which propagates over the sample and couples out at hole $i$. $r_{ij}$ is the distance between the holes; $\phi_{ij}$ is the angle between the incoming polarization and the direction of plasmon propagation.*

Using equation 5 as our model for the plasmon-assisted transmission, we calculate the indirect contribution $\langle |E_s|^2 \rangle$ to the mean intensity:

$$\left\langle |E_s|^2 \right\rangle = \sum_j^N \left\langle \frac{|A_0(\phi_j)|^2}{r_j} e^{-2(\sigma\rho + l_{abs}^{-1})r_j} \right\rangle = \frac{\rho \left\langle 2\pi \left|A_0(\phi)\right|^2 \right\rangle_\phi}{2(\sigma\rho + l_{abs}^{-1})} \tag{6}$$

This expression contains a single sum since the plasmon contributions have random phases and amplitudes so that contributions from different holes are statistically independent and average out to zero. The summation is subsequently approximated by an integral over an infinite number of holes: $\sum_{holes} = \int_0^{2\pi} \mathrm{d}\phi \int_0^\infty \rho r \mathrm{d}r$. Equation 6 shows that at high densities, all excited plasmons are fully scattered out as visible light and then $\langle |E_s|^2 \rangle$ becomes a constant; at low densities, most plasmons are absorbed into the sample and $\langle |E_s|^2 \rangle$ scales linearly with $\rho$.

## 2.3 Transmission correlation

In the previous sections we have shown that the transmission of light through a sample with randomly spaced holes produces a speckle pattern that is due to both direct and plasmon-mediated contributions. We expect the two contributions to show a distinct wavelength-dependent behaviour. Therefore, studying the correlation of the speckle patterns as a function of wavelength will allow us to separate and analyze them.

We define the correlation of the transmitted intensity at different wavelengths as follows:

$$C \equiv \frac{\left\langle I(\lambda_0, \vec{\theta}_0) I(\lambda_1, \vec{\theta}_1) \right\rangle}{\left\langle I(\lambda_0, \vec{\theta}_0) \right\rangle \left\langle I(\lambda_1, \vec{\theta}_1) \right\rangle} - 1 \tag{7}$$

We may write the correlation in terms of fields using Isserliss' theorem for Gaussian random independent variables [20]:

$$C = \frac{\left| \left\langle E(\lambda_0, \vec{\theta}_0) E^*(\lambda_1, \vec{\theta}_1) \right\rangle \right|^2}{\left\langle I(\lambda_0, \vec{\theta}_0) \right\rangle \left\langle I(\lambda_1, \vec{\theta}_1) \right\rangle} \tag{8}$$

We continue our calculations assuming $k_{||}(\lambda_0) = k_{||}(\lambda_1)$, simplifying the calculation because all phase factors $e^{i\vec{k}_{||}(\lambda_0)\cdot\vec{r} - i\vec{k}_{||}(\lambda_1)\cdot\vec{r}}$ are then equal to one. Moreover, this choice prevents the correlation function from decaying rapidly with wavelength [21]. To account for this premise in our experiments we must correlate the speckle patterns under a far-field angle $\vec{\theta}$ that varies with wavelength as:

$$k_{||} = 2\pi \cdot \frac{\sin(|\vec{\theta_0}|)}{\lambda_0} = 2\pi \cdot \frac{\sin(|\vec{\theta_1}|)}{\lambda_1} \tag{9}$$

We now rewrite the numerator in equation 8 in terms of the direct and indirect fields, similarly to equation 3:

$$\left|\left\langle E(\lambda_0,\vec{\theta}_0)E^*(\lambda_1,\vec{\theta}_1)\right\rangle\right|^2 = N\left[\langle E_d(\lambda_0)E_d^*(\lambda_1)\rangle + \langle E_s(\lambda_0)E_s^*(\lambda_1)\rangle\right], \tag{10}$$

Assuming $E_d$ to be wavelength-independent, the first term in this expression reduces to $|E_d|^2$. The second term can be evaluated using the plasmon model described in the previous section, analogously to equation 6. We assume that neither the coupling and excitation efficiency $A_0(\phi)$, nor the scattering cross section $\sigma$, nor the absorption length $l_{abs}$ depend strongly on wavelength. We rewrite the difference of the real parts of the plasmon wave number, Re $[k_{\text{spp}}(\lambda_0) - k_{\text{spp}}(\lambda_1)]$, to $2\pi\text{Re}\left[\frac{n_{\text{eff}}(\lambda_0)}{\lambda_0} - \frac{n_{\text{eff}}(\lambda_1)}{\lambda_1}\right] \approx 2\pi\text{Re}\,\overline{n}_{\text{eff}}\frac{\Delta\lambda}{\lambda_0\lambda_1}$ where the only approximation is that Re $n_{\text{eff}}(\lambda_0) \approx$ Re $n_{\text{eff}}(\lambda_1) \approx$ Re $\overline{n}_{\text{eff}}$ is a constant, so that Re $k_{\text{spp}} = \frac{2\pi\text{Re}\,\overline{n}_{\text{eff}}}{\lambda_1}$. We take Re $\overline{n}_{\text{eff}}$ to be the average of Re $n_{\text{eff}}(\lambda)$ over the total wavelength range and determine its theoretical value using the complex indices of refraction of N-BK7 Schott glass and gold studied by E.D. Palik [22] and E.W. Johnson et al [23]. The second term in equation 10 is then:

$$\langle E_s(\lambda_0)E_s^*(\lambda_1)\rangle = \left\langle |E_s|^2\right\rangle \frac{\widetilde{\lambda}}{\widetilde{\lambda} + i\Delta\lambda} \text{ where } \widetilde{\lambda} \equiv (\sigma\rho + l_{abs}^{-1})\frac{2\lambda_0}{\text{Re } k_{\text{spp}}} \tag{11}$$

For a wavelength detuning $\Delta\lambda = \lambda_1 - \lambda_0$ of zero from the reference wavelength $\lambda_0$, this expression is equal to equation 6; it now includes a complex Lorentzian factor that depends on the wavelength detuning. The width of the Lorentzian is given by $\widetilde{\lambda}$, which is proportional to the plasmonic losses; note that $\widetilde{\lambda}$ is not a constant, but depends linearly on $\lambda_0\lambda_1$.

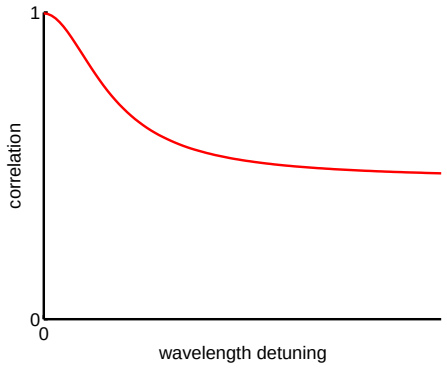


*Figure 4: Example of the theoretical intensity correlation as a function of wavelength detuning for the transmission of a sample with randomly spaced subwavelength holes. The correlation function consists of a Lorentzian part and a constant background.*

Combining the above results yields the speckle pattern correlation as a function of wavelength detuning:

$$C = \frac{1}{\langle I_{tot}\rangle^2}\left|\langle I_d\rangle + \frac{\langle I_s\rangle\widetilde{\lambda}}{\widetilde{\lambda} + i\Delta\lambda}\right|^2 \tag{12}$$

where $\langle I_d\rangle = |E_d|^2$ is the ensemble averaged direct transmission (see equation 3), $\langle I_s\rangle$ is the ensemble averaged plasmon-mediated transmission (see equation 6), and $\langle I_{tot}\rangle = \langle I_s + I_d\rangle$ is the ensemble averaged total transmission. The correlation function is a Lorentzian with a constant background as shown in figure 4, which is set by two parameters. The first is the width of the Lorentzian ($\widetilde{\lambda}$) which is proportional to the plasmonic losses:

$$\text{loss } = \sigma\rho + l_{abs}^{-1} = \frac{\text{Re } k_{\text{spp}}}{2\lambda_0}\widetilde{\lambda} \tag{13}$$

In our experiments, the theoretical minimum of $\widetilde{\lambda}$ is typically about 5 nm; we therefore need a wavelength resolution under 5 nm to resolve the Lorentzian. The second parameter that describes the correlation function is the constant background, which is set by the ratio of indirect and direct contributions to the transmitted intensity $\frac{\langle I_s\rangle}{\langle I_d\rangle}$. From equation 6 we see that this intensity ratio is given by:

$$\text{intensity ratio} = \frac{\langle I_s\rangle}{\langle I_d\rangle} = \frac{1}{\langle I_d\rangle}\frac{\rho\left\langle 2\pi\left|A_0(\phi)\right|^2\right\rangle_\phi}{2(\sigma\rho + l_{abs}^{-1})} \tag{14}$$

In conclusion, we can study the plasmonic loss and the intensity ratio by measuring experimental correlation functions and fitting them with the model in equation 12. The loss and intensity depend strongly on the hole density $\rho$, and the correlation function changes accordingly. The loss and therefore the Lorentzian width increases with density; the intensity ratio also increases with density, which is seen as a decreasing background correlation.

For completeness, note that equations 11 and 12 are not true Lorentzians in the wavelength detuning $\Delta\lambda$, but in the parameter $\frac{\Delta\lambda}{\lambda_0\lambda_1}$ or equivalently the frequency detuning $\Delta\omega$. This corresponds to the Lorentzian-type resonances of the form $\frac{1}{\widetilde{\omega}-i\Delta\omega}$ that we are familiar with from standard literature, which are also given in the frequency domain. This form follows naturally from the Fourier-transform of an exponential decay in time, as frequency and time are a Fourier-related pair.

## 2.4 Non-plasmon surface waves

In the previous sections, we have assumed that the surface wave-assisted transmission through a sample with randomly spaced holes is only due to surface plasmons. However, previous theory [13, 14] and experiments [13, 15] have shown that the total evanescent field radiated by a hole can be decomposed into three fields, which describe the behaviour of the evanescent field at short, intermediate and long distances: these are termed the quasicylindrical wave, the surface plasmon wave, and the Norton wave respectively. The quasicylindrical wave, whose field decays more quickly than the exponentially decaying plasmon field, contributes significantly to the total surface wave field at distances under 2 plasmon wavelengths [13]. The Norton wave, whose field decays algebraically and thus more slowly than the plasmon field, contributes significantly to the total field at distances beyond 9 plasmon propagation lengths [13]. If we encounter contributions of non-plasmon surface waves in our experiments, we expect to see them as follows. At low hole densities (large distances), a Norton wave contribution will cause the intensity ratio of surface wave-assisted to direct transmission to become larger; additionally, the surface wave losses will decrease since the Norton field decays more slowly than the plasmon field. At high hole densities (short distances), a quasicylindrical wave contribution will cause the intensity ratio to increase; the surface wave losses will also increase since the quasicylindrical field decays more quickly than the plasmon field.

# 3 Experimental setup

The goal of our experimental setup is to image the far-field transmission of a sample with a random pattern of subwavelength holes onto a camera. Subsequently, we wish to vary the wavelength of the incident light. By calculating the correlation of the resulting speckle patterns as a function of wavelength, we can then compare our experimental correlation functions to our theoretical expectations. In this Chapter we explain how we reach our experimental goal by addressing the following five requirements of the setup: a suitable sample (discussed in section 3.1); a narrow band of light with a tunable wavelength (section 3.2); a wavelength-independent beam shape (section 3.3); correct imaging of the far-field transmission of the sample (section 3.4); and automated measurements (section 3.5).

## 3.1 Samples

For our experiment, we use a gold film perforated with random patterns of subwavelength holes. SEM images of two representative samples are shown in figure 5. The samples consist of three layers: a glass substrate; a gold layer (150 nm); and a chrome layer (20 nm). The chrome layer damps plasmons on the gold-air interface, allowing analysis of plasmons on the gold-glass interface only [18]. All samples are 400 $\mu$m by 400 $\mu$m wide and are positioned on the same slab to ensure a uniform thickness of the gold layer. We characterize the samples using two parameters: the hole shape, which is either square (side length = 125 $\pm$ 5 nm) or circular (diameter = 120 $\pm$ 6 nm), and the average sample area per hole, which is $qa_0^2$ where $a_0$ = 450 nm and $q \in$ [1, 2, 3, 4, 9, 16, 25, 36, 81, 144]. Because it is computationally demanding to generate random patterns, the densest patterns have been created by repeating a single disordered array of 100 $\mu$m by 100 $\mu$m. This breaking of disorder limits the size of the beam incident on the sample to 100 $\mu$m by 100 $\mu$m [17]. For calibration purposes, we also have samples with ordered patterns of circular subwavelength holes with a rectangular cell structure of sides $a_0$ and $qa_0$, where $q \in$ [6, 7, 8, 9, 10, 12]. This is the same sample collection that was used in previous work [18, 17].

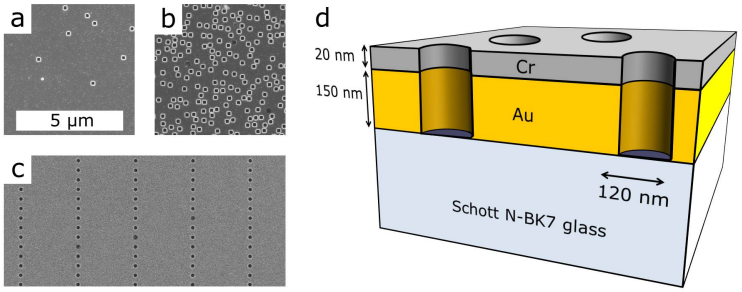


*Figure 5: SEM images of three of the studied samples and a schematic representation of the sample layer structure. (a),(b) Two of our set of twenty random samples, with densities 0.20 $\mu m^{-2}$ and 4.9 $\mu m^{-2}$ respectively. (c) One of our set of six ordered samples with a rectangular cell structure of sides $a_0$ and $6a_0$ where $a_0$ = 450 nm. (d) Sample layer structure.*

## 3.2 Filtering the laser light

A schematic picture of our experimental setup is shown in figure 6. The setup consists of three parts, A, B and C, as indicated in the figure. In this section we discuss part A, where we filter a supercontinuum light source to a bandwidth of approximately 1 nm and make the light tunable over a wavelength range of roughly 100 nm.

Our supercontinuum light source is a fianium WhiteLase SC-340-2 laser. The laser emits coherent light over a wavelength range in excess of 400-2000 nm with an average spectral power density of >1 mW/nm [24]. The output divergence of the laser is strongly wavelength-dependent and therefore the output of the laser is difficult to focus. This issue is resolved by pre-filtering the laser light to a band of roughly 100 nm using a set of longpass and shortpass filters.

We use a Jarrell-Ash 82-410 monochromator to filter the laser light to a tunable wavelength and a narrow bandwidth. The linear dispersion of this monochromator is specified as 3.3 nm/mm [25]. Hence, to obtain the desired bandwidth of 1 nm, the incident beam diameter must be approximately 300 $\mu$m. We use lens M (f = 750 mm) to focus the laser beam onto the entrance of the monochromator. The available power in the laser beam after the monochromator is

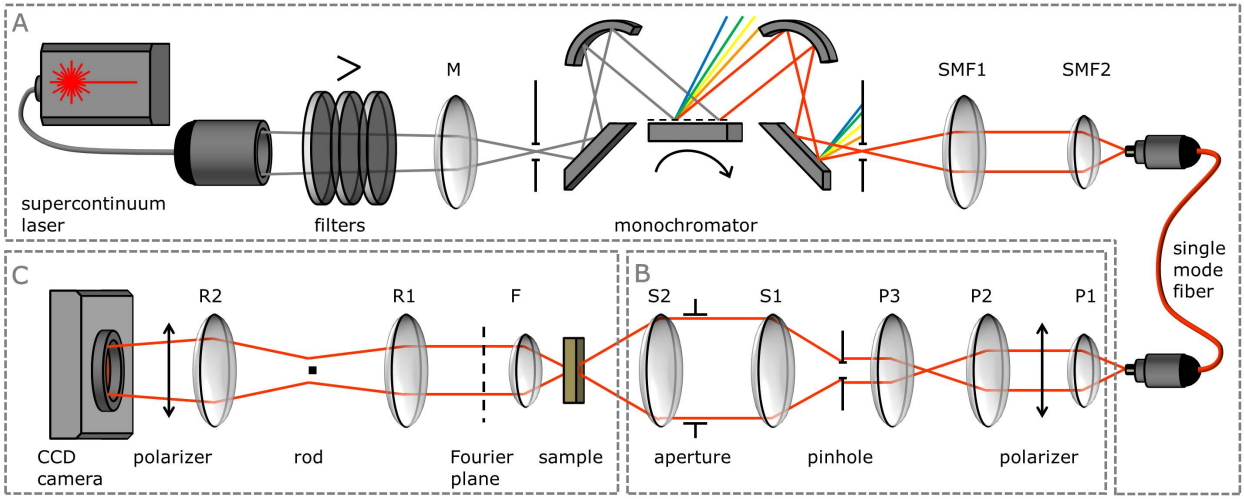


*Figure 6: Top view of the experimental setup, which consists of three parts: (A) reduction of the bandwidth and wavelength tuning of the laser light; (B) shaping the light to an appropriate size and profile; (C) imaging the far-field transmission of the sample. In part A, the beam of our supercontinuum source is filtered and subsequently imaged onto the entrance of the monochromator via lens M. The output of the monochromator is imaged onto a single mode fiber via lenses SMF1 and SMF2. In part B, the light coupled out of the single mode fiber passes through a linear polarizer and illuminates a pinhole via lenses P1, P2 and P3. The pinhole is imaged onto the sample via lenses S1 and S2. In part C, a Fourier-transform of the illuminated sample is imaged onto a camera using lenses F, R1 and R2. A rod blocks the zeroth-order transmission of the sample. An analyzing polarizer may be placed before the camera.*

roughly 150 $\mu$W.

Lenses SMF1 (f = 500 mm) and SMF2 (f = 8 mm) image the exit slit of the monochromator onto a single mode fiber, where the magnification is chosen such that the beam diameter matches the mode field diameter of the fiber. Using an OceanOptics USB2000+ spectrometer with a resolution of 1 $\pm$ 0.1 nm, we measure the bandwidth of the single mode fiber output to be 1.8 $\pm$ 0.3 nm. This bandwidth provides us with the resolution needed to determine changes in the far-field transmission due to wavelength tuning (see Chapter 2). The power in the laser beam behind the single mode fiber is 10-50 $\mu$W.

## 3.3 Shaping the laser beam

In part B of the setup shown in figure 6 we image a spot onto our sample that is <100 $\mu$m in diameter and which size does not depend on wavelength. To this end, we illuminate a pinhole with the output of the single mode fiber using lenses P1 (f = 8 mm), P2 (f = 250 mm) and P3 (f = 50 mm), where P1 collimates the fiber output and P2 and P3 reduce the output beam diameter. A linear polarizer is placed between lenses P1 and P2. The pinhole is imaged onto the sample using lenses S1 (f = 200 mm) and S2 (f = 75 mm), resulting in a spot diameter on the sample of $\sim$ 75 $\mu$m. An adjustable aperture on lens S2 reduces the numerical aperture of this lens to 0.09 $\pm$ 0.02 to block light from the pinhole incident at large angles.

We choose to use a pinhole for the following reason: when the single mode fiber output is imaged onto the sample, the spot size will increase with wavelength [26]. Hence, the beam spot will illuminate different holes in the sample during wavelength tuning, an effect which is not incorporated in our theoretical model. By contrast, the image of an illuminated pinhole on the sample is practically constant with wavelength if the illuminating spot is larger than the pinhole. Thus, using an illuminated pinhole results in a trade-off between power and constant spot size. We have chosen the magnification of P2 and P3 such that only half of the beam power is cut away by the pinhole. The intensity at the edges of the pinhole is then 50% of the intensity at the center and the power of the light incident on the sample is 5-25 $\mu$W. Note that the reduced numerical aperture of lens S2 re-introduces a small wavelength

dependence to the spot diameter on the sample; however, this effect is modest since the diffraction introduced by the cutoff corresponds to about 10 % of the spot diameter.

## 3.4 Imaging the far-field transmission

In part C of the setup, as indicated in figure 6, we image the far-field transmission of the sample onto an Apogee Alta U1 CCD camera. Here, the challenge is to place the sample in the front focal plane of Fourier-transforming lens F(f = 8 mm) and at the same time to image the back focal plane of lens F onto the CCD camera. It is not possible to image the far-field transmission of the sample directly onto the camera: firstly, the Fourier plane is not physically accessible to the camera; secondly, the zeroth-order transmission of the sample needs to be blocked, since it is roughly $10^3$ times more intense than the speckle pattern we wish to measure. Therefore we use a relay system consisting of two lenses. The first relay lens R1(f = 100 mm) images the back focal plane of lens F onto a blocking rod. The second relay lens R2(f = 75 mm) then images the rod and the speckle pattern onto the CCD camera. A linear analyzing polarizer may be placed before the camera to do polarization-dependent measurements. Unless indicated otherwise, the measurements presented are performed without this polarizer.

To ensure that all planes are correctly aligned, we use the following procedure. Assume that relay lens R2, the blocking rod, relay lens R1, Fourier-transforming lens F, the sample, and lens S2 are not yet placed. We start by placing the blocking rod. We then add lens R2 to image the blocking rod onto the camera. The sample is then placed at about 42 cm from the blocking rod, and we introduce lens F to image the sample onto the blocking rod. Then we add S2 to image the pinhole onto the sample. We can now calculate the positions of the front and back focal planes of F with respect to the sample, using the object and image distances in this configuration and the technical specifications of F. The distance of the sample to the front focal plane is 150 $\pm$ 5 $\mu$m, and the distance between the focal planes of F is 17.46 mm (which also takes into account the effective thickness of the lens). We then remove lens F and move the sample 17.61 mm towards the blocking rod to the calculated position of the back focal plane of F. We add lens R1 to image the sample onto the blocking rod. We then move the sample to the calculated position of the front focal plane of F, which is 150 $\mu$m closer to F than the initial position of the sample. F is then returned to the setup. As the last step, S2 is moved toward the sample by 150 $\mu$m to image the pinhole onto the sample. The Fourier plane of the sample is now imaged onto the camera with a magnification of 1.06 $\pm$ 0.05.

## 3.5 Automation

We have automated the wavelength tuning of the laser light and the capturing of camera images. To this end, we use a Newport ESP300 Motion Controller/Driver system in conjunction with LabVIEW to control the dial on the monochromator and the shutter on the camera. We have calibrated the wavelength of the monochromator using a Helium-Neon laser and an OceanOptics USB2000+ spectrometer. We have also checked the linearity of the wavelength with the dial on the monochromator, using a white light source and the USB spectrometer.

In our experiments, we use a wavelength scan range of 690-790 nm. Within this scan range, an image of the far-field transmission is taken after each wavelength step of 1 nm. We adjust the integration time for each image such that 50-60% of the saturation level of the camera is reached; typical integration times range from 0.01-10 s per image. After scanning over the wavelength range, a dark measurement of corresponding integration time is taken for each image and subsequently subtracted.

# 4 Data analysis method

In this Chapter, we address how we analyze the recorded speckle patterns to produce experimental correlation functions that we subsequently compare to our theoretical model. First we describe the data analysis method (section 4.1). We explain that to correlate the speckle patterns, we must first rescale them as a function of wavelength, reflecting our theoretical premise that we compare intensities at different wavelengths at the same value of $k_{||}$ (see Chapter 2). A data analysis challenge is presented (section 4.2): we found that the image of the Fourier plane on the camera is slightly deformed. Investigation of this imaging deformation using the transmission of samples with ordered hole patterns yields deviations up to 3% with respect to perfect imaging. We explain that we subsequently solve this issue by changing the way in which we rescale our speckle patterns (section 4.3).

## 4.1 Processing speckle patterns

We wish to compare the correlation of the recorded speckle patterns as a function of wavelength detuning to our theoretical model for the correlation function (see Chapter 2). In this model, we correlate the transmitted far-field intensities at different wavelengths, but at the same value of $k_{||}$ (see equation 9):

$$k_{||} = 2\pi \cdot \frac{\sin(|\vec{\theta_0}|)}{\lambda_0} = 2\pi \cdot \frac{\sin(|\vec{\theta_1}|)}{\lambda_1} \tag{15}$$

where $\lambda$ is the wavelength and $\vec{\theta}$ is the far-field angle. At this value of $k_{||}$, we subsequently perform an ensemble average to obtain an expression for the correlation function. In our experiments, we correlate the transmitted intensities at different wavelengths by comparing the speckle patterns pixel by pixel and approximating ensemble averaging by averaging over the speckles. Most importantly, each position within our recorded speckle patterns corresponds to a decreasing value of $k_{||}$ for increasing wavelengths. This relationship between image position and $k_{||}$-value is partially defined by equation 15, which relates $k_{||}$ to $\vec{\theta}$; and partially by the specifications of our imaging setup as indicated in figure 7, which allow us to relate $\vec{\theta}$ to $\vec{r}$. The corresponding imaging formula is:

$$\tan(|\vec{\theta}|) = \frac{|\vec{r}|}{M \cdot f(\lambda)} \tag{16}$$

where $\vec{r}$ is the position in the Fourier plane; $\vec{\theta}$ is the far-field angle; $f(\lambda)$ is the wavelength-dependent focal length of lens F; and $M$ is the magnification of the imaging system.

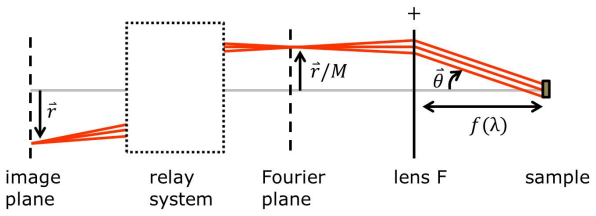


*Figure 7: Schematic of the imaging setup (part C in figure 6), where the far-field transmission of the sample is imaged. $\vec{r}$ Indicates the position in the plane; $\vec{\theta}$ is the angle between the ray diffracted from the sample and the optical axis; $f(\lambda)$ is the wavelength-dependent focal length of lens F; and $M$ is the magnification of the imaging system.*

To correlate recorded speckle pattern images analogously to the theory, we must therefore rescale the images at all wavelengths such that corresponding pixels in different images have identical values of $k_{||}$. We perform the rescaling procedure as follows. We first choose a speckle image $\alpha$ at wavelength $\lambda_\alpha$ as the rescaling reference for the remaining images $\{\beta\}$ at wavelengths $\{\lambda_\beta\}$. Given position $\vec{r}_\alpha$ in speckle image $\alpha$ at wavelength $\lambda_\alpha$, we calculate the corresponding value of $k_{||}$ using equations 15 and 16. We then calculate the position $\vec{r}_\beta$ in speckle image $\beta$ at wavelength $\lambda_\beta$ that corresponds to the same value of $k_{||}$. Schematically:

$$|\vec{r}_\alpha| \xrightarrow{eq.16\ ,\ eq.15} k_{||} \xrightarrow{eq.15\ ,\ eq.16} |\vec{r}_\beta| \tag{17}$$

For illustration, in figure 8 we show two areas at wavelengths $\lambda_\alpha$ (690 nm) and $\lambda_\beta$ (790 nm) where corresponding positions $\vec{r}_\alpha$ and $\vec{r}_\beta$ have the same values of $k_{||}$. The last step is to create a rescaled version $\beta_{new}$ of speckle pattern $\beta$, where the speckle pattern intensity value at $\vec{r}_\beta$ in the unscaled image is moved to $\vec{r}_{\beta\ new} = \vec{r}_\alpha$ in the rescaled

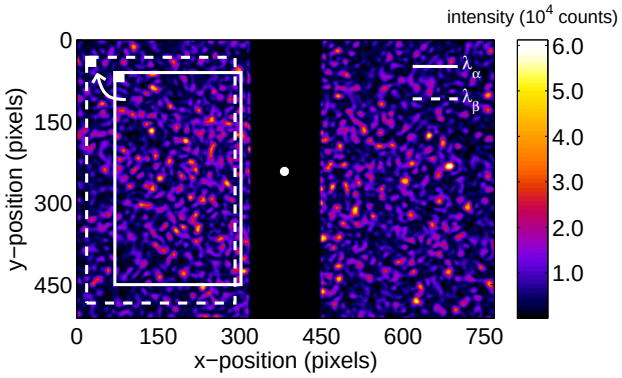


*Figure 8: Example of areas in a speckle pattern at two different wavelengths with identical values of $k_{||}$ at corresponding positions. Shown here is a false-colour CCD image (resolution: 9 $\mu$m/pixel) of the far-field transmission through a sample with randomly spaced sub-wavelength holes. The white circle indicates the location of the zeroth-order transmission, which is blocked by the black rod. The white solid outline indicates the reference area at initial wavelength $\lambda_\alpha$ = 690 nm. The white dashed outline indicates the corresponding area at final wavelength $\lambda_\beta$ = 790 nm. The white corner boxes indicate two positions of identical $k_{||}$ for wavelengths $\lambda_\alpha$ and $\lambda_\beta$ respectively.*

image for each value of $\vec{r}_\alpha$. The resulting collection of rescaled speckle patterns $\{\beta_{new}\}$ has the same values of $k_{||}$ at each pixel as speckle pattern $\alpha$.

We subsequently use the rescaled images to calculate the correlation of the speckle pattern image at a reference wavelength with respect to the images at increasing wavelength detuning, using matrix correlation as was done in previous work [17]. In this way we obtain an experimental correlation function as a function of wavelength detuning.

## 4.2 Imaging challenges

So far, the way in which we rescale our speckle patterns assumes perfect imaging of the far-field transmission of the sample onto the camera; however, we experimentally find small deviations from a perfect imaging system in our setup. To correctly compare our data to the theoretical model, we therefore need to characterize the image deformation and adapt our image rescaling to compensate for this deformation.

We investigate the deformation along the x-axis of our image using the diffraction orders of the transmission of ordered samples. An example of the far-field transmission of an ordered sample is shown in figure 9. Using a 2-D Gaussian fit, we determine the positions of the diffraction orders along the x-axis. We can then compare the measured order positions to their expected positions in the case of perfect imaging (when $\sin(|\vec{\theta}|) = \frac{m\lambda}{qa_0}$ for the $m^{th}$ order), as a function of three parameters: the position along the x-axis of our image; the wavelength; and the distance between Fourier-transforming lens F and the sample.

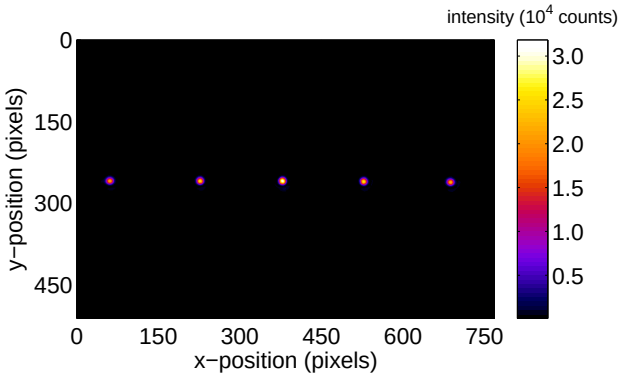


*Figure 9: False-color CCD image (resolution: 9 $\mu$m/pixel) of the far-field transmission of an ordered array of sub-wavelength holes as described in Chapter 3. We use the position of the transmission orders to characterize imaging deformations in our setup along the x-axis.*

In figure 10a, we plot the measured versus the expected diffraction order positions along the x-axis of the image at a wavelength of 690 nm to qualify the deformation as a function of position. On the scale in this figure, the imaging appears to be linear and thus perfect. However, fitting with a quadratic function $x_{measured} = a + b \cdot x_{expected} + c \cdot x^2_{expected}$ yields a small quadratic dependence $a = 379.2 \pm 0.8$, $b = 1.024 \pm 0.003$, $c = 6 \cdot 10^{-5} \pm 2 \cdot 10^{-5}$, implying some deformation. Here, $a$ is the position of the zeroth-order transmission, $b$ is a correction on the magnification M previously indicated in figure 7, and $c$ indicates an asymmetric deformation which stretches the image left of the

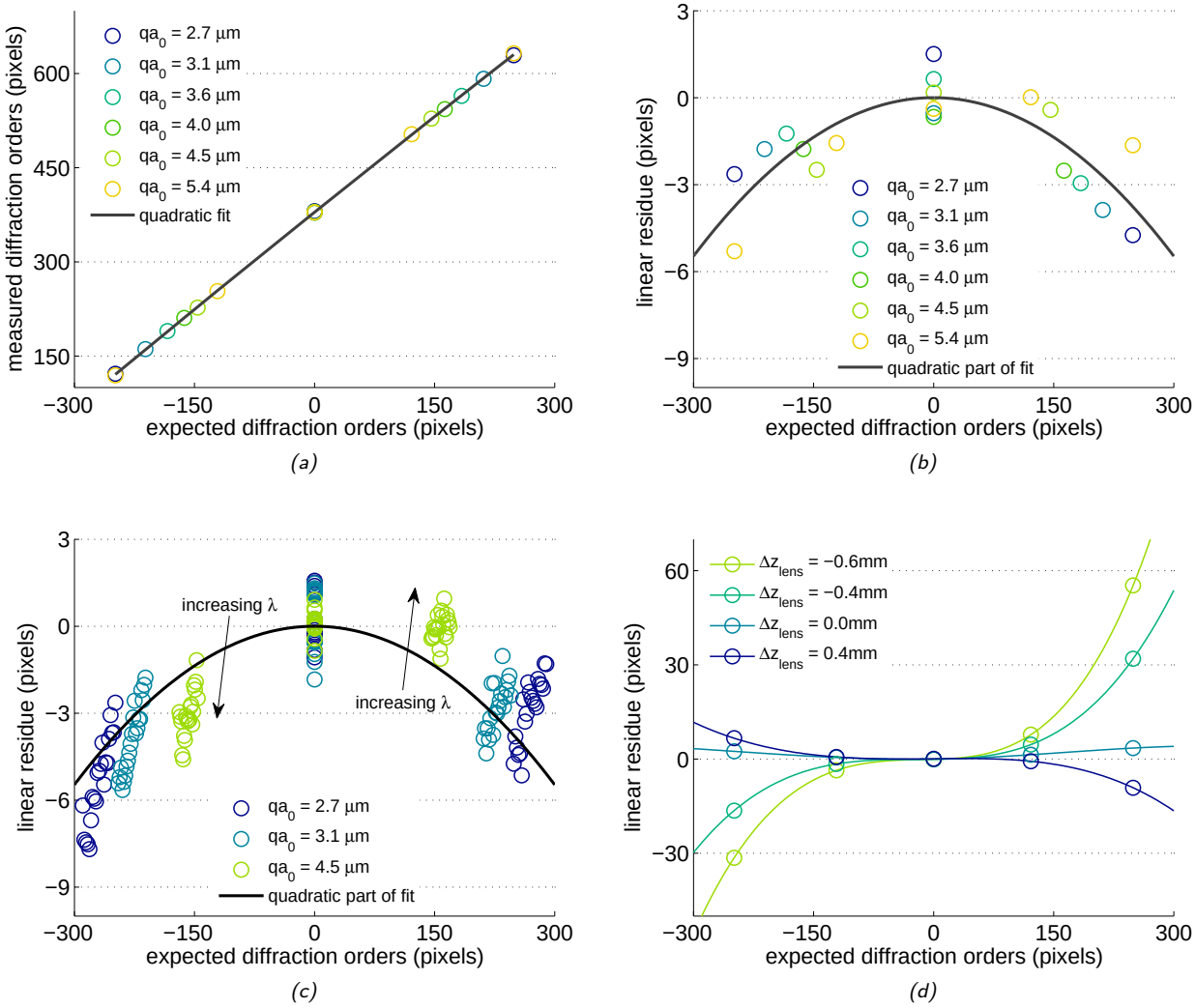


*Figure 10: Characterization of image deformation using diffraction orders of ordered samples imaged onto the CCD camera. (a) Position-dependent deformations: measured positions of diffraction orders versus expected positions at wavelength 690 nm. On this scale, their relation looks linear, indicating perfect imaging. The fitted line is quadratic. (b) Position-dependent deformations: residue of the measured positions of diffraction orders at 690 nm with respect to the linear part of the quadratic fit in (a), expected for perfect imaging. The position-dependent deformations vary up to 6 pixels. (c) Wavelength-dependent deformations: residue of measured positions of diffraction orders with respect to the linear part of the quadratic fit in (a) at 690 nm, for multiple wavelengths between 690 nm and 790 nm. The wavelength-dependent deformations vary up to 8 pixels. (d) Lens position-dependent deformations: residue of measured positions of diffraction orders at various distances between the Fourier-transforming lens and the sample (relative to the optimum distance $\Delta z_{lens} = 0$) with respect to a linear fit at the optimum distance. The lines are a guide to the eye. The deformations vary strongly with the lens position, increasing up to 30 pixels at 0.4 mm from the optimum.*

zeroth-order and shrinks the image right of the zeroth-order. To get a better overview of the size of this deformation, we subtract the linear part of the fit from the data and plot the residue along with the quadratic part of the fit in figure 10b. We see that the deformation has a maximum of about 6 pixels over a range of 300 pixels, or 2%. The data have a random scatter of roughly 2 pixels, caused by asymmetric fringes in the intensity profiles of the diffraction orders, which make center positions difficult to determine using a simple 2-D Gaussian fit.

We then investigate the wavelength dependence of the deformation by plotting the positions of the measured and expected diffraction orders for multiple wavelengths between 690 and 790 nm. To keep a good overview over the

data, we subtract the linear part of the fit at 690 nm from our data and plot the resulting residue in figure 10c , analogously to figure 10b. Here, we see that there is an additional wavelength dependence of the deformation, with a maximum deformation of about 8 pixels over a range of 300 pixels, or 3%. Once more the data have a random scatter of roughly 2 pixels.

Lastly, we study whether the deformation depends on the distance between the Fourier-transforming lens F and the sample. To quantify this deformation, we plot the measured and expected positions of the diffraction orders at a wavelength of 690 nm for various distances between lens and sample that deviate from the optimum distance. To keep a good overview, we again show the residue of the measured positions with respect to a linearly fitted function that represents perfect imaging. The result is shown in figure 10d. We can see that the deformations depend strongly on the alignment of lens F (f = 8 mm), deforming between 10 and 30 pixels over a range of 300 pixels, or 3 to 10%, at only 0.4 mm from the optimum lens position. At the optimum lens position, the residue has a quadratic shape indicating an asymmetric deformation similar to figure 10b which stretches the image right of the zeroth-order and shrinks the image left of the zeroth-order. At non-optimum lens positions, the residue can be approximated by a cubic function which indicates a position-dependent magnification that is symmetric around the zeroth-order, and additional higher-order terms that indicate further deformations. We cannot use the diffraction orders as a guide to align this lens, because the alignment precision of the lens is too small.

## 4.3 Imaging solutions

Although we have qualified the deformations that our speckle patterns are subject to, it is not possible to precisely quantify them and incorporate them directly into the rescaling method we use for the speckle patterns. There are two reasons for this: first of all, the scatter in our data is nearly of the same order of magnitude as the deformation we try to quantify, and therefore any model will have a large error margin; secondly, the deformations depend strongly on the alignment of the setup, varying as much as 6 pixels between alignments. Therefore, instead of using one rigid characterization of the deformation, we use dynamic adaptation during rescaling based on the assumption that deformation can only lead to decorrelation and that therefore the rescaling that leads to the highest correlation best reflects the deformations.

We perform dynamic rescaling to compensate for image deformations by subdividing a large correlating area into an array of small areas of approximately 100 by 100 pixels. For each small area and each wavelength we use the standard rescaling method described in section 1, and additionally shift the reference image along the x- and y-axes to maximize the correlation. We subsequently average the correlation over these areas. Effectively, this method adjusts the position of the speckle pattern to compensate for deformations. This rescaling method provides the following advantages: firstly we perform a rescaling iteration for each wavelength, which means we are able to filter out part of the wavelength-dependent deformation; and secondly the use of small correlating areas ensures that we compensate for a part of the position-dependent aberrations.

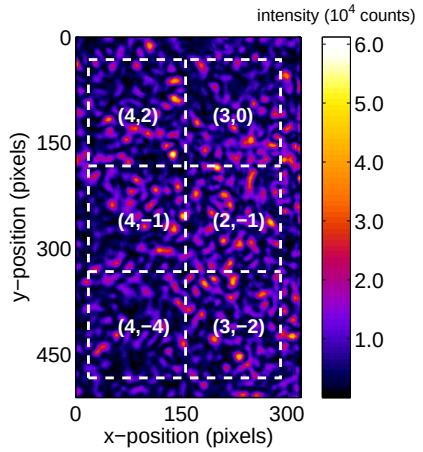


*Figure 11: Example of dynamic rescaling of correlating areas in a speckle pattern as discussed in section 3. Shown here are correlating areas at 100 nm wavelength detuning from the reference. Displayed in each area is the shift ($\Delta x$,$\Delta y$) along the x- and y-axes required for the corresponding reference area to maximize the correlation.*

The effect of dynamic rescaling on our experimental correlation functions depends on the quality of the alignment

of the setup, which largely dictates the character of the image deformations. On average, using dynamic rescaling prevents 3-15% decorrelation at 100 nm wavelength detuning. The required shift of the reference areas is comparable in size to the deformations presented in figure 10 and varies from -5 to $+5$ pixels, where the sign and size of the shift qualifies the type of deformations in our image. For comparison, the average speckle size is roughly 15 by 15 pixels. In figure 11 a representative example is shown of correlating areas in a speckle pattern, along with the shift of their respective reference areas over 100 nm wavelength detuning. As an example, we take a closer look at the bottom left corner area: the reference area shift of $(\Delta x, \Delta y) = (4, -4)$ indicates that the reference area has been shifted 4 pixels to the right and 4 pixels upward in the speckle image. Effectively, this shift increases the distance between the reference and correlating area when compared to a zero shift (perfect imaging). This fits with the type of deformations seen in figure 10b, which imply that the leftmost side of the images is stretched.

# 5 Results

In this Chapter, we test our model (see Chapter 2) which describes the correlation of the far-field transmission of a metal-dielectric sample with randomly spaced subwavelength holes as a function of wavelength detuning. We present our experimental correlation functions and fit them with the model (section 5.1). We study the correlation functions for different hole densities, where we expect to see both the plasmon contributions and the plasmonic losses to increase with density due to increased scattering. Subsequently we address issues encountered while fitting the correlation functions and our solutions to these challenges (section 5.2). If there is a good correspondence between correlation model and data, we can extract the plasmonic losses and the ratio of surface wave and direct contributions to the transmitted intensity from the fit parameters. We plot the experimental losses and intensity ratios as a function of hole density (sections 5.3 and 5.4) and fit these functions with our models derived in Chapter 2. This analysis allows us to extract the plasmon absorption length and the scattering cross section of the holes. We then present an overview of the parameters extracted from our measurements (section 5.5).

## 5.1 Correlation functions

In figure 12 we show representative examples of our experimental correlation functions with their fitted models (equation 12 and 18). The correlation functions are extracted from speckle patterns recorded in the wavelength range 690-790 nm, using samples with square holes of hole densities 4.9, 1.6, and 0.55 $\mu$m$^{-2}$ respectively. The reference wavelength, which corresponds to a wavelength detuning of 0 nm, is chosen at 690 nm. The correlation functions show the density-dependent behaviour that we expect (see Chapter 2): the width of the correlation peak increases with density, indicating larger plasmonic losses; and the background correlation decreases with density, indicating a larger relative contribution from plasmon-assisted transmission. For each hole density, we see that

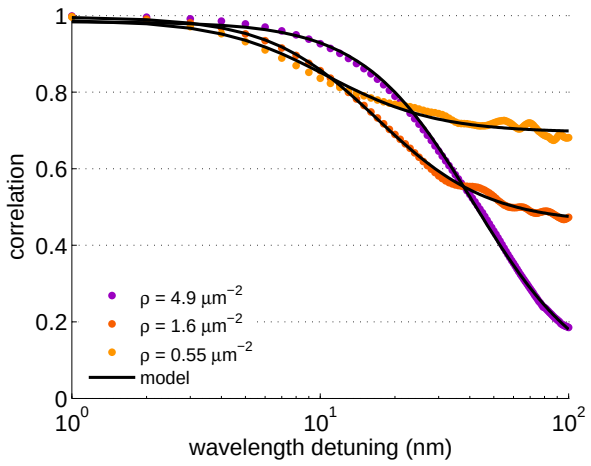


*Figure 12: Examples of experimental correlation functions and their fitted models (eq. 12). The correlation functions shown are measured in the wavelength range 690-790 nm for samples of hole densities 4.9, 1.6 and 0.55 $\mu$m$^{-2}$ respectively using a reference wavelength of 690 nm.*

the fitted model and the experimental correlation function correspond well. The model is described in Chapter 2, equation 12:

$$C = \frac{1}{\langle I_{tot}\rangle^2}\left|\langle I_d\rangle + \frac{\langle I_s\rangle\,\widetilde{\lambda}}{i\Delta\lambda + \widetilde{\lambda}}\right|^2 \tag{18}$$

This function is a Lorentzian with a constant background correlation. It is described by two parameters: the first is the width of the Lorentzian ($\widetilde{\lambda}$), which is proportional to the plasmonic scattering and absorption losses; the second is the background correlation, which is set by the ratio of surface wave and direct contributions to the transmitted intensity ($\langle I_s\rangle$ and $\langle I_d\rangle$). We fit equation 12 to the data in a least-squares sense using the plasmonic losses and the background correlation as free parameters. In addition, we use a third fit parameter that allows the normalized direct and surface wave contributions to the intensity not to add up to 1. This parameter compensates for noise in the correlation at the reference wavelength.

It is important to note that the shape of the correlation function, which is set by the plasmonic loss and the intensity ratio, is largely determined around its reference wavelength. This is due to the fact that the decorrelation width, which is typically less than 25 nm, is much smaller than the scan range of 100 nm. This wavelength dependence is illustrated in figure 13, where we plot two correlation functions calculated from the same experimental data (measured for a sample with square holes and hole density 0.55 $\mu$m$^{-2}$) but with reference wavelengths chosen at 690 and 790 nm respectively. Using these two reference wavelengths therefore allows us to see the wavelength dependence of the plasmonic loss and the intensity ratio.

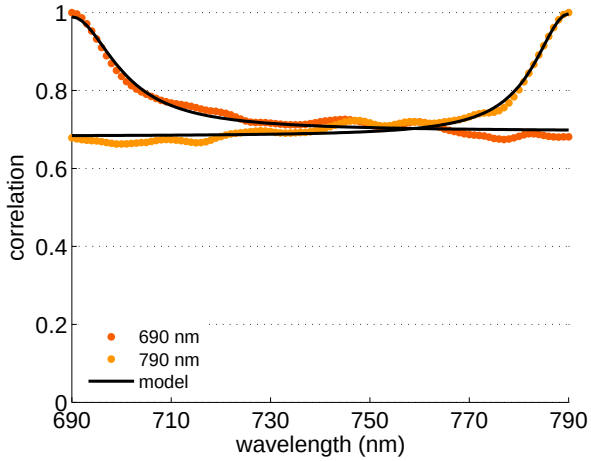


*Figure 13: Correlation functions calculated from the same experimental data measured for a sample of hole density 0.55 $\mu m^{-2}$ starting either at reference wavelength 690 nm or at 790 nm; their shape is largely determined around the respective reference wavelengths.*

## 5.2 Fitting challenges

We encounter two challenges during the fitting procedure of the correlation functions. These are illustrated in figure 14, where we plot correlation functions measured for samples with square holes and with reference wavelength 690 nm. Firstly, for samples of low hole densities the correlation functions decorrelate with increasing wavelength detuning by an amount that is comparable to the height of the correlation peak, instead of stabilizing at a constant background correlation. Such decorrelation is demonstrated in figure 14 for a sample with hole density $\rho = 0.06$ $\mu$m$^{-2}$. It may be caused by wavelength dependencies that are not accounted for in our theory or not correctly compensated for in our setup. The decorrelation causes the Lorentzian part of the correlation function to be misrepresented as an oscillation by our fitted model. We solve this issue by fitting the Lorentzian width of the correlation function over a wavelength range of only 40 nm instead of 100 nm, since we thereby effectively cut away the decorrelating background. We always perform this procedure for the lower hole densities $\rho \in$ [0.31, 0.20, 0.14, 0.06, 0.03] $\mu$m$^{-2}$; for measurements on samples with round holes and reference wavelength 790 nm we also apply it to higher

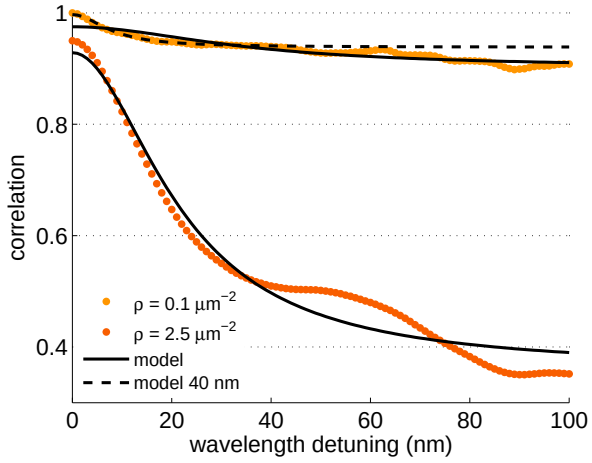


*Figure 14: Example of decorrelation and oscillations in experimental correlation functions and their effect on the fitted model. At $\rho = 0.06$ $\mu m^{-2}$ we see a large decorrelation with wavelength detuning relative to the height of the Lorentzian peak. Over a fitting range of 100 nm (solid line), this leads to a misrepresentation of the Lorentzian width; over a range of 40 nm (dashed line) the width is well fitted. The correlation at $\rho = 2.5$ $\mu m^{-2}$ (shifted downward by 0.05 for clarity) shows large oscillations, which lead to a large error margin on the fitted model. We attribute this effect to statistical errors due to the finite number of speckles.*

hole densities $\rho \in$ [0.55, 1.2, 1.6, 2.5] $\mu$m$^{-2}$, to ensure the widths are well fitted.

Secondly, all correlation functions show oscillations with a period comparable to the Lorentzian width, and a maximum amplitude of 0.05 correlation points. An extreme example is shown in figure 14 for a sample of hole density $\rho =$ 2.5 $\mu$m$^{-2}$; the correlation function is shifted down by 0.05 correlation points for clarity. The oscillations arise since we calculate the correlation by averaging over a limited number of speckles instead of using ensemble averaging, as described in Chapters 2 and 4. The correlation oscillations lead to larger error margins on the fitted model. We reduce this problem to a minimum by maximizing the correlation areas in our speckle patterns.

## 5.3 Plasmonic absorption and scattering losses versus hole density

Since the experimental correlation functions and the fitted model correspond well, we can extract the plasmonic losses and intensity ratios from the fit parameters. In this section we present the resulting experimental losses as a function of hole density and compare them to the models described in Chapter 2.

In Chapter 2, equation 13 we demonstrated that the plasmonic losses are proportional to the width $\widetilde{\lambda}$ of the correlation function:

$$\text{loss } = \sigma\rho + l_{abs}^{-1} = \frac{\text{Re } k_{\text{spp}}}{2\lambda_0}\widetilde{\lambda} \tag{19}$$

This expression shows that the losses have a density-dependent part due to scattering and a density-independent offset due to absorption. Since our samples have a wide range of hole densities, we may be able to separate the two loss contributions. We fit the model to the experimental losses versus hole density in a least-squares sense, leaving the scattering cross section $\sigma$ and the absorption length $l_{abs}$ as free parameters.

In figure 15 we present plasmonic losses as a function of hole density as extracted from correlation functions in three datasets (measured using distinct experimental parameters) and their fitted models. The data in figure 15a were obtained for samples with square holes and a reference wavelength of 690 nm; in figure 15b, square holes and a reference wavelength of 790 nm were used; and for the data in figure 15c samples with round holes and reference wavelength 690 nm were used. For all datasets, we see that there is a very good agreement between data and model. We can therefore extract the scattering cross sections $\sigma$ and the plasmon absorption lengths $l_{abs}$ from the fits. However, in figures 15a and 15b we see that the plasmonic loss value for the highest hole density deviates significantly from the model. This deviation was also reported previously [17, 18] as an effect of the quasicylindrical wave, and we have therefore chosen not to include the loss values for the highest hole density in any of the fits.

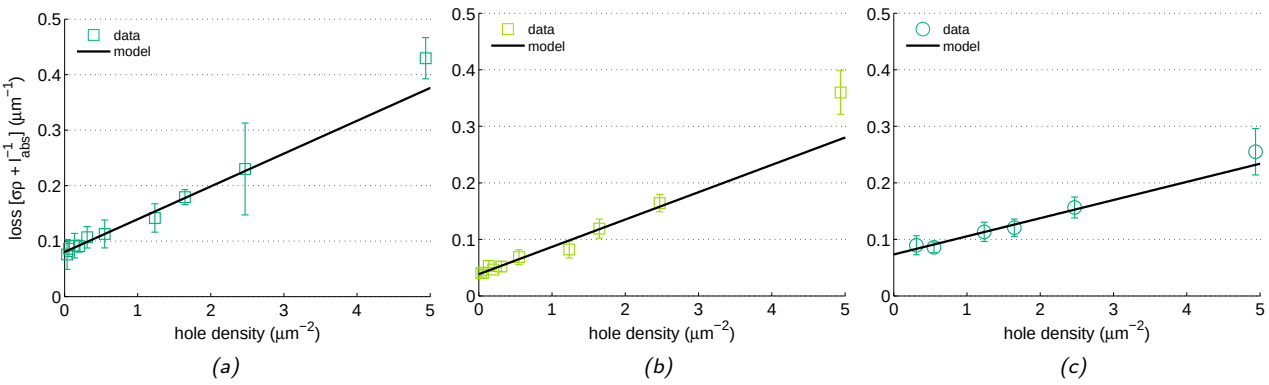


*Figure 15: Experimental plasmonic losses as a function of hole density, extracted from three datasets with distinct experimental parameters, along with their fitted models (eq. 13). We show the loss versus hole density extracted from experimental correlation functions measured for: (a) samples with square holes and reference wavelength 690 nm; (b) samples with square holes and reference wavelength 790 nm; (c) samples with circular holes and reference wavelength 690 nm.*

Firstly we discuss the scattering cross section $\sigma$, which is equal to the slope of the loss as a function of hole density (see equation 19). From the presented datasets we extract the following values of $\sigma$ : for square holes and reference wavelength 690 nm, we find 59 $\pm$ 6 nm (figure 15a); for square holes and reference wavelength 790 nm, it is 48 $\pm$ 7 nm (figure 15b); and for round holes and reference wavelength 690 nm, we find 30 $\pm$ 10 nm (figure 15c). These cross sections are roughly twice as small as the side length of the square holes (125 $\pm$ 5 nm) and roughly four times as small as the diameter of the round holes (120 $\pm$ 6 nm). We thus conclude that the cross section $\sigma$ depends strongly on the hole shape, increasing by roughly a factor two from round to square holes. Comparing the slopes of the data in figure 15a (reference wavelength 690 nm) and figure 15b (reference wavelength 790 nm), $\sigma$ also appears to be wavelength-dependent; however, this dependence is not statistically significant. Lastly, it is interesting to note that the $\sigma$ found in previous work, using the same method and samples in a wavelength range of 740-810 nm [17, 18], were 26 $\pm$ 2 nm for square holes and 18 $\pm$ 1 nm for round holes; our values of $\sigma$ are significantly larger for both hole types.

Secondly we investigate the plasmon absorption length $l_{abs}$, which is the inverse of the axis cutoff of the loss as a function of hole density (see equation 19). From the presented datasets we extract $l_{abs}$ to find: 12 $\pm$ 1 $\mu$m for square holes and reference wavelength 690 nm (figure 15a); 26 $\pm$ 5 $\mu$m for square holes and reference wavelength 790 nm (figure 15b); and 13 $\pm$ 3 $\mu$m for round holes and reference wavelength 690 nm (figure 15c). The value of $l_{abs}$ thus increases by a factor of roughly two going from reference wavelength 690 nm to 790 nm, indicating that the absorption length is wavelength dependent. In addition, the extracted absorption length does not depend on hole shape. This corresponds to the theoretical expectation that $l_{abs}$ is a geometry-independent property which depends only on sample materials and wavelength. To compare the experimental and theoretical absorption lengths, we calculate $l_{abs}$ at a glass-gold interface (see figure 16) using the wavelength-dependent complex indices of refraction of N-BK7 Schott glass and gold, studied by E.D. Palik [22] and E.W. Johnson et al [23]. At 690 nm, the theoretical value of $l_{abs}$ is 8-13 $\mu$m; at 790 nm $l_{abs}$ it is 22-24 $\mu$m. Both values correspond within the error margins to the experimental absorption lengths at reference wavelengths 690 nm and 790 nm respectively. Note that in previous work [17, 18] $l_{abs}$ at 740 nm was found to be 20.4 $\pm$ 0.8 $\mu$m for square holes and 29 $\pm$ 2$\mu$m for round holes. Contrary to our findings, these data yielded the unphysical result that $l_{abs}$ depends significantly on hole shape. In addition, the absorption length found previously for round holes does not correspond well to the theoretical value (see figure 16).

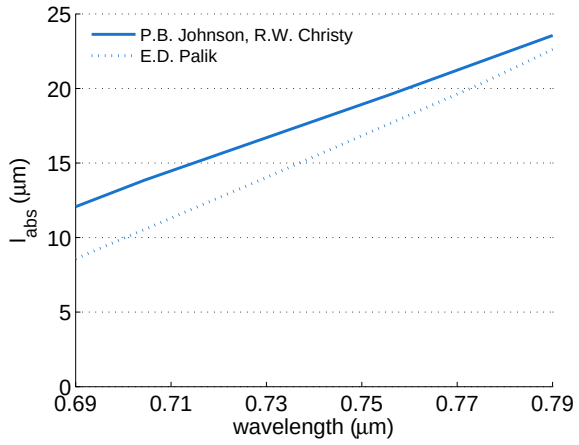


*Figure 16: Theoretical values of the propagation length of surface plasmons on a gold-glass interface, calculated using the complex refractive indices of N-BK7 Schott glass and gold (studied by E.D. Palik [22] and P.B. Johnson et al. [23] respectively).*

## 5.4 Ratio of surface wave to direct contributions versus hole density

We also extract the ratios of the surface wave contribution to the direct contribution to the transmitted intensity from the fit parameters of the correlation models and plot them as a function of hole density. In Chapter 2, equation 14 we derived the following expression for the intensity ratio:

$$\text{intensity ratio } = \frac{\langle I_s \rangle}{\langle I_d \rangle} = \frac{1}{2\langle I_d \rangle} \cdot \frac{\rho \langle 2\pi \left| A_0(\phi) \right|^2 \rangle_\phi}{\sigma\rho + l_{abs}^{-1}} \equiv \frac{A\rho}{\sigma\rho + l_{abs}^{-1}} \tag{20}$$

This model is fitted in a least-squares sense to the experimental intensity ratios versus hole density on a double logarithmic scale. We insert the values of $l_{abs}$ and $\sigma$ extracted from the plasmonic losses versus hole density, leaving

only $A$ as a free parameter.

In figure 17 we present the intensity ratios as a function of hole density as extracted from correlation functions in four datasets measured using distinct experimental parameters, and their fitted models. The data in figure 17a were obtained for samples with square holes and reference wavelengths 690 nm and 790 nm respectively; in figure 17b, samples with round holes and reference wavelengths 690 nm and 790 nm were used. For all datasets shown, we see that there is a reasonable agreement between data and model over roughly one order of magnitude of the hole density. However, the intensity ratio at the highest hole density deviates significantly from the model for all datasets, and we have therefore chosen not to include these intensity ratios in the fitted data.

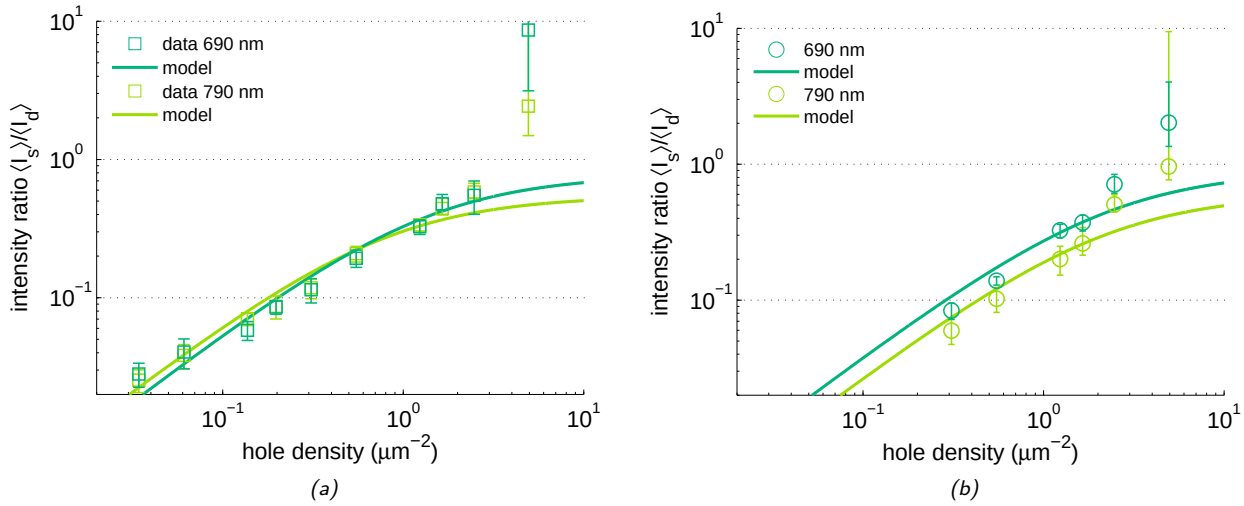


*Figure 17: Experimental intensity ratios of surface wave and direct contributions as a function of hole density, along with their models (eq. 14 and eq. **??**). The data presented are extracted from four datasets with distinct experimental parameters. We show the loss versus hole density extracted from experimental correlation functions measured for: (a) samples with square holes and reference wavelengths 690 nm and 790 nm; (b) samples with round holes and reference wavelengths 690 nm and 790 nm.*

First we examine the deviations between data and model at high and low densities. As discussed in Chapter 2, the plasmon model is valid at intermediate hole densities; at high and low densities we may see contributions of the quasicylindrical and Norton wave [13] to the total surface wave field. Firstly, in literature [14, 16] it was demonstrated that for the highest hole density we likely see a contribution of the quasicylindrical wave. This wave contributes up to 2 plasmon wavelengths from a hole; on a gold-glass interface with incident wavelength 690 nm, the maximum contribution distance is about 1 $\mu$m. For the highest density and square holes with scattering cross section 60 nm, the distance at which $(1 - \frac{1}{e})$ of the plasmon field is scattered out is $(\sigma\rho)^{-1} \approx 3.5$ $\mu$m. So over roughly one third of the scattering length the quasicylindrical wave contributes significantly to the total scattered field, and hence it is plausible that this wave is responsible for the increased intensity ratio. Secondly, the Norton wave is expected to contribute significantly beyond 6 plasmon absorption lengths from a hole; at 690 nm where $l_{abs} \approx 12$ $\mu$m, this translates to a minimum contribution distance of about 110 $\mu$m. Since the total surface wave must propagate over at least this distance for the Norton wave to contribute significantly to the total scattered field, the Norton wave will only be seen for samples with a scattering length $(\sigma\rho)^{-1}$ larger than 110 $\mu$m. This condition is met by the two least dense samples with square holes, since their scattering distances $(\sigma\rho)^{-1}$ are roughly 500 and 270 $\mu$m. Therefore, we may see a Norton wave contribution to the intensity ratios at the two lowest densities for square holes and reference wavelength 690 nm (shown in figure 17a).

Lastly, comparing figures 17b and 17a shows that the intensity ratios for samples with square holes remain the same at reference wavelengths 690 nm and 790 nm, but that the intensity ratios for samples with round holes decrease by a factor of roughly 0.7. This decrease is illustrated in figure 18 where we show two correlation functions calculated from the same experimental data (measured for a sample with round holes and hole density 1.6 $\mu$m$^{-2}$) but with

reference wavelengths chosen at 690 nm and 790 nm. The background correlation is larger at 790 nm than at 690 nm, which indicates that the ratio of surface wave to direct contributions decreases with wavelength. It is not clear why the intensity ratio depends on wavelength for samples with round holes but not for square holes. In this context it is interesting to note that the direct transmission of identical samples has been measured previously [16]. It was found that for round holes the directly transmitted intensity is asymmetric from 690 to 790 nm, decreasing by a factor 0.7, but for square holes it is roughly symmetric, peaking around 750 nm and decreasing by a factor 0.9 at 690 and 790 nm. Similarly, the intensity ratios for round holes are not the same under reversal of the reference wavelength, but the intensity ratios for square holes are. Some of these observations might be explained by shape resonances [27].

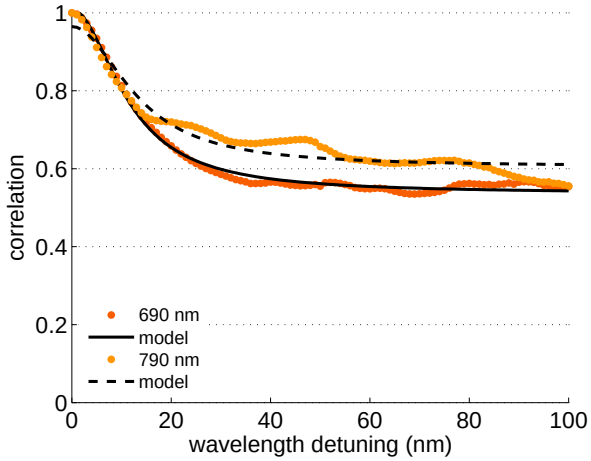


*Figure 18: Example of the decreasing intensity ratio with wavelength for samples with round holes. Shown are two correlation functions calculated from the same experimental data (hole density: 1.6 $\mu m^{-2}$) but starting at reference wavelengths 690 nm and 790 nm; the background correlation is higher for 790 nm than for 690 nm, indicating that the intensity ratio of surface wave to direct intensity contributions decreases with wavelength.*

We now formulate two simple expectations for the wavelength dependence of the intensity ratios for round holes. We find that neither scenario reflects the experimental decrease of the intensity ratio with wavelength, implying that the indirect contribution to the intensity ratio decreases more strongly with wavelength than expected. For both scenarios, we assume that the intensity ratio can be approximated by $\frac{\langle I_s \rangle}{\langle I_d \rangle} \propto \frac{1}{\langle I_d \rangle} \langle |A(\phi)|^2 \rangle \rho l_{abs}$, which means we must take into account the absorption length which increases by a factor 2 over 690 to 790 nm. In the first scenario, we assume that the direct field decreases from 690 to 790 nm by a factor $\sqrt{0.7}$ [16]; and that the indirect field follows this trend so that $\langle |A(\phi)|^2 \rangle$ decreases by a factor $\sqrt{0.7}^2$ from 690 to 790 nm, where we square the effect to account for both excitation and outcoupling of the surface waves. These considerations yield an intensity ratio that is expected to increase from 690 to 790 nm by a total factor of roughly 1.7. In the second scenario, we assume that the direct field is proportional to $\lambda^{-2}$ (Bethe approximation, [12]), thus decreasing by a factor 0.8 from 690 to 790 nm; and that the indirect field is proportional to $\lambda^{-4}$, so that $\langle |A(\phi)|^2 \rangle$ decreases by a factor 0.6 from 690 to 790 nm. This scenario yields an expected increase of the intensity ratio over the 690-790 nm range by a factor 1.5.

## 5.5 Overview of results

In the previous sections we have discussed selected representative experimental results; in table 1 we give an overview of all performed measurements, presenting the experimental values of the hole scattering cross section $\sigma$ and the plasmon absorption length $l_{abs}$. For comparison, we have also included the experimental results from previous work, using the same method and samples in a wavelength range of 740-810 nm [17, 18]. Our measurements are separated into datasets characterized by their experimental parameters: a round or square hole shape; a parallel orientation of the analyzing polarizer or no analyzing polarizer; and a reference wavelength of 690 or 790 nm. Note that all data presented so far have been measured without an analyzing polarizer. The data in table 1 indicate that the presence of the analyzing polarizer has little effect on the results. The data therefore confirm the results of the previous sections: we find that the absorption length is only dependent on wavelength; the scattering cross section appears to have a wavelength- and polarization-dependence that is statistically not yet significant, but varies most strongly with hole shape.

| dataset | measurement details | | | | extracted parameters | |
|---|---|---|---|---|---|---|
| | hole shape | samples used | analyzing polarizer | reference wavelength (nm) | $l_{abs}$ ($\mu$m) | $\sigma$ (nm) |
| 1 | square | 10 densest | none | 690 | 12 ± 1 | 59 ± 6 |
| 2 | square | 10 densest | none | 790 | 26 ± 5 | 48 ± 7 |
| 3 | square | 8 densest | parallel | 690 | 14 ± 4 | 80 ± 20 |
| 4 | square | 8 densest | parallel | 790 | 27 ± 19 | 60 ± 30 |
| 5 | round | 6 densest | none | 690 | 13 ± 3 | 30 ± 10 |
| 6 | round | 6 densest | none | 790 | 25 ± 3 | 18 ± 3 |
| 7 | round | 6 densest | parallel | 690 | 13 ± 3 | 40 ± 10 |
| 8 | round | 6 densest | parallel | 790 | 22 ± 8 | 20 ± 10 |
| [17, 18] | square | 10 densest | parallel | 740 | 20.4 ± 0.8 | 26 ± 2 |
| [17, 18] | round | 5 densest | parallel | 740 | 29 ± 2 | 18 ± 1 |

*Table 1: Extracted values of the plasmonic absorption length $l_{abs}$ and scattering cross section $\sigma$ for each of the eight datasets with distinct experimental parameters measured in this experiment. Also shown are experimental results from previous work, using the same method and samples in a wavelength range of 740-810 nm [17, 18].*

# 6 Concluding discussion

In this thesis we have presented research in which we study surface waves (most importantly surface plasmon polaritons, and also quasicylindrical waves and Norton waves) at a metal-dielectric interface. To this end, we have studied the correlation of speckle patterns as a function of wavelength detuning. These speckle patterns are seen when illuminating samples with randomly spaced subwavelength holes. We have presented a simple theoretical model for the correlation function, which predicts that we can separate the light transmitted directly through the holes from the light transmitted indirectly via surface plasmons. This model also predicts that we can extract the plasmonic losses and the intensity ratio between the direct and indirect processes from the correlation function.

We have seen these expectations confirmed in the experimental correlation functions, which agree very well with the simple theoretical model. From these correlation functions, we have subsequently extracted the plasmonic losses and the intensity ratios as a function of hole density. The wavelength-dependent plasmonic absorption length and the scattering cross sections of the holes were successfully extracted from the plasmonic losses. The absorption lengths found correspond very well to their predicted values. In addition, the intensity ratios measured for the densest samples are dramatically higher than predicted by our model. We attribute this result to a contribution of the quasicylindrical wave to the total surface wave field. At the lowest densities, the intensity ratios show a small increase that may be attributable to the Norton wave; however, this increase can also be due to measurement errors. In conclusion, our research has shown that the method of transmission correlation for samples with randomly spaced holes is a good method to study the properties of surface waves.

It is important to note that our theoretical model for the correlation, as discussed in Chapter 2, assumes many parameters in the experiment to be approximately wavelength-independent. Most significantly, the absorption length $l_{abs}$ (fitted with the model), the direct contribution to the transmitted intensity $I_d$ (also fitted with the model), and the real part of the effective refractive index Re $n_{\text{eff}}$ (included in the model as a constant) are assumed to be constant within the scanned wavelength range. Even though these approximations generally work well, we have seen in Chapter 5 that the absorption length does depend on wavelength. We have also seen that the correlation functions and corresponding intensity ratios found for round holes depend significantly on wavelength, which can be at least partially ascribed to the wavelength-dependence of the directly transmitted intensity. In addition, the real part of the effective refractive index depends non-negligibly on wavelength as can be calculated using the wavelength-dependent complex indices of refraction of N-BK7 Schott glass and gold, studied by E.D. Palik [22] and E.W. Johnson et al [23]. Therefore, future goals to obtain more accurate results are to reconsider the relative weight of the correlating wavelengths in the fitting procedure, and to extend our simple model to include the theoretical wavelength-dependence of Re $n_{\text{eff}}$.

Within several months, the experiments described in this thesis will be repeated for different wavelength ranges between 500 and 900 nm. We hope that these measurements will yield information about the wavelength-dependence of surface plasmon properties. Additionally, we thereby wish to further study the contribution to the total surface wave field of the Norton wave at low densities and of the quasicylindrical wave at high densities. We are also interested to what extent our simple theoretical model for the correlation will hold in different wavelength ranges.

# References


[1] R. H. Ritchie. *Plasma losses by fast electrons in thin films*, Phys. Rev. **106**, 874 (1957).

[2] W.L. Barnes, A. Dereux, T.W. Ebbesen. *Surface plasmon subwavelength optics*, Nature **242**, 824 (2003)

[3] A. Otto. *Excitation of nonradiative surface plasma waves in silver by the method of frustrated total reflection*, Z. Phys. **216**, 398 (1968).

[4] E. Kretschmann, H. Raether. *Radiative decay of non-radiative surface plasmons excited by light*, Z. Naturf. A **23**, 2135 (1968).

[5] R. H. Ritchie, E. T. Arakawa, J. J. Cowan, R. N. Hamm. *Surface-plasmon resonance effect in grating diffraction*, Phys. Rev. Lett. **21**, 1530 (1968).

[6] P. A. Fedders. *Indirect coupling of photons to the surface plasmon*, Phys. Rev. **165**, 580 (1968)

[7] R. Zia, J. A. Schuller, M. L. Brongersma. *Plasmonics: the next chip-scale technology*, Materials Today **9**, 20 (2006).

[8] A. Polman, H. A. Atwater. *Plasmonics: optics at the nanoscale*, Materials Today **8** 56 (2005).

[9] J. Homola, S. S. Yee, G. Gauglitz. *Surface plasmon resonance sensors: review*, Sensors Actuat. B *54*, 3 (1999).

[10] M. L. Brongersma, P. G. Kik. *Surface plasmon nanophotonics*, Springer, New York (2007)

[11] T.W. Ebbesen, H.J. Lezec, H.F. Ghaemi, T. Thio, P.A. Wolff. *Extraordinary optical transmission through sub-wavelength hole arrays*, Nature **391**, 667 (1998)

[12] H.A. Bethe. *Theory of diffraction by small holes*, Phys. Rev. **66**, 163 (1944)

[13] A.Y. Nikitin, F.J. García-Vidal, L. Martín-Moreno. *Surface electromagnetic field radiated by a subwavelength hole in a metal film*, Phys. Rev. Lett **105**, 073902 (2010)

[14] H. Liu, P. Lalanne. *Microscopic theory of the extraordinary optical transmission*, Nature **452**, 728 (2008)

[15] P. Lalanne, J.P. Hugonin. *Interaction between optical nano-objects at metallo-dielectric interfaces*, Nat. Phys. **2**, 551 (2006).

[16] F. van Beijnum, C. Rétif, C.B. Smiet, M.P. van Exter. *Transmission proceses in random patterns of subwavelength holes*, Opt. Lett. **38**, 3666 (2011)

[17] J. Sirre. *Analysis of speckles behind random nano holes (Master thesis)*, Leiden University (2011).

[18] F. van Beijnum, J. Sirre, C. Rétif, M.P. van Exter. *Speckle correlation functions applied to surface plasmons*, Phys. Rev. B **85**, 035437 (2012).

[19] L. Yin, V. K. Vlasko-Vlasov, J. Pearson, J. M. Hiller, J. Hua, U. Welp, D. E. Brown, C. W. Kimball. *subwavelength focusing and guiding of surface plasmons*, Nano Lett. **5**, 1399 (2005)

[20] L. Isserliss. *On a formula for the product-moment coefficient of any order of a normal frequency distribution in any number of variables*, Biometrika **12**, 134 (1918).

[21] O.L. Muskens, T. van der Beek, A. Lagendijk. *Theory of diffraction by small holes*, Phys. Rev. B **84**, 035106 (2011)

[22] E.D. Palik. *Handbook of optical constants of solids*, Academic Press, Orlando (1985)

[23] P. B. Johnson, R. W. Christy. *Optical constants of the noble metals*, Phys. Rev. B **6**, 4370 (1972)

[24] Fianium. *WhiteLase SC400 & SC450 High-Power Supercontinuum data sheet*, (2012). Available at: http://www.fianium.com/pdf/whitelasesc400.pdf (accessed 29-6-2012)

[25] Jarrell-Ash Company. *Operating instructions for the 0.25 meter Ebert monochromator*, (1967). Available at: https://wiki.brown.edu/confluence/download/attachments/29406/Jarrell+Ash.pdf (accessed 19-6-2012)

[26] Thorlabs. *Single Mode Patch Cables: FC/PC to FC/PC*, Volume 21 Catalog, p. 1006 (2011). Available at: http://www.thorlabs.com/catalogpages/V21/1006.PDF (accessed 3-7-2012)

[27] K.L. van der Molen, K.J. Klein Koerkamp, S. Enoch, F. B. Segerink, N. F. van Hulst, L. Kuipers. *Role of shape and localized resonances in extraordinary transmission through periodic arrays of subwavelength holes: Experiment and theory*, Phys. Rev. B **72**, 045421 (2005)